

Diagnosing the sensitivity of grounding line flux to changes in sub-ice shelf melting

Tong Zhang¹, Stephen Price¹, Matthew Hoffman¹, Mauro Perego², and Xylar Asay-Davis¹

¹Fluid Dynamics and Solid Mechanics Group, Los Alamos National Laboratory, Los Alamos, NM, 87545, USA

²Center for Computing Research, Sandia National Laboratories, Albuquerque, NM, 87185, USA

Correspondence: T. Zhang (tzhang@lanl.gov)

Abstract. Motivated by previous work using ice flow models to quantify the impacts of ice shelf buttressing on grounding line flux (e.g., Fürst et al., 2016; Reese et al., 2018), we look for an improved physical understanding for how ice dynamics link ice thickness perturbations, via changes in sub-ice shelf melting, to changes in ice shelf buttressing and grounding line flux. More specifically, we seek to define one or more “metrics” that are 1) readily calculated from standard ice sheet model outputs and 2) informative with respect to diagnosing the sensitivity of grounding line flux to changes in ice thickness at specific locations on an ice shelf. By studying the ice dynamics for both idealized (MISMIP+) and realistic (Larsen C) ice shelves, we find a strongly direction-dependent buttressing number that links local changes in ice shelf thickness and dynamics with changes in the integrated grounding line flux. This buttressing metric, defined using the first principal stress, is better overall for quantifying changes in grounding line flux than a similar metric defined using the second principal stress or stress along the flow direction. This correlation is possibly controlled by the relative relationship of geometric/dynamic features between the perturbation point and the grounding line, indicating a dynamic (time evolving) sensitivity field of grounding line flux change to basal melt. Unfortunately, this metric only shows a robust relationship with the integrated grounding line flux for regions near the center of an ice shelf; for points too near the grounding line or the calving front, no clear relationship exists between any of the readily calculable metrics explored here and changes in grounding line flux. This motivates our exploration of an adjoint-based method for defining grounding line flux sensitivity to local changes in ice shelf geometry. When using the same idealized case, we demonstrate that this adjoint-based method is equivalent to the sensitivity analysis of (Reese et al., 2018) while requiring only a single model adjoint solve. We conclude that adjoint-based methods provide a powerful and efficient tool for determining the grounding line flux sensitivity to changes in sub-ice shelf melting.

Copyright statement. TEXT

20 1 Introduction

Marine ice sheets like West Antarctica (and to a lesser extent, portions of East Antarctica) are grounded below sea level and their bedrock would remain so even after full isostatic rebound (Barletta et al., 2018). This and the fact that ice sheets generally

thicken inland lead to a geometric configuration that are prone to instability; a small increase in flux at the grounding line thins the ice there, leading to floatation, a retreat of the grounding line into deeper water, further increases in flux (due to still thicker ice), and further thinning and grounding line retreat. This theoretical “marine ice sheet instability” mechanism (Mercer, 1978; Schoof, 2007) is supported by idealized (e.g., Schoof, 2012; Asay-Davis et al., 2016) and realistic (e.g., Cornford et al., 2015; Royston and Gudmundsson, 2016) ice sheet modeling experiments and some studies (Joughin et al., 2014; Rignot et al., 2014) argue that such an instability is currently under way along outlet glaciers of Antarctica’s Amundsen Sea Embayment (ASE). The relevant perturbation for grounding line retreat in the ASE is thought to be intrusions of relatively warm, intermediate-depth ocean waters onto the continental shelves, which have reduced the thickness and extent of marginal ice shelves via increased submarine melting (e.g., Jenkins et al., 2016). These reductions are critical because fringing ice shelves restrict the flux of ice across their grounding lines farther upstream—the so-called “buttressing” effect of ice shelves (Gudmundsson et al., 2012; Gudmundsson, 2013; De Rydt et al., 2015)—which makes them a critical control on the rate of ice flux from Antarctica to the ocean.

On ice shelves, gradients in hydrostatic pressure are balanced primarily by the extensional flow of ice towards the calving front (Hutter, 1983; Morland, 1987; Schoof, 2007) and, in theory, an ice shelf in one horizontal dimension (x - z) provides no buttressing (Schoof, 2007; Gudmundsson, 2013). For realistic, three-dimensional ice shelves however, buttressing results from three main sources: 1) compressive ice flow, 2) lateral shear, and 3) “hoop” stress (Pegler and Worster, 2012). Both compressive and lateral shear stresses can supply backward resistance to extensional ice shelf flow through along-flow and across-flow stress gradients, while hoop stress is a transverse stress arising from azimuthal extension in regions of diverging flow (Wearing, 2016). Due to the complex geometries, kinematics, and dynamics of real ice shelves, an understanding of the specific processes and locations that control ice shelf buttressing is far from straightforward.

Several recent studies apply whole-Antarctic ice sheet models, optimized to present-day observations, towards improving our understanding for how Antarctic ice shelves limit flux across the grounding line (and by extension how they impact ice dynamics farther inland). Fürst et al. (2016) calculated the buttressing across Antarctica ice shelves along two major directions (aligned with the ice flow and with the second principal stress) and evaluated their impacts on upstream ice dynamics to identify regions of the ice shelves that are dynamically “passive”; in these regions increased submarine melting, or even complete removal of the ice should not significantly alter local or regional ice dynamics or the flux of ice upstream. Reese et al. (2018) used perturbation experiments to link small, localized decreases in ice shelf thickness to changes in integrated grounding line flux (GLF), thereby providing a map of GLF sensitivity to local increases in submarine melt rates. Goldberg et al. (2019) assessed the consistency of satellite retrieved and modeled melt rates, found the importance of bathymetry in influencing the ice sheet responses predicted by models and also investigated the adjoint sensitivity of volume above floatation to melt rates for Dotson and Crosson ice shelves, Antarctica.

Steve to update this paragraph to better reflect what we actually do below: 1) connect the studies of Fürst and Reese by trying to understand if / how local evaluations of ice shelf buttressing do or do not reflect the actual potential for perturbations at those same locations to impact the flux across the GL (since that is, presumably, why we care about buttressing in the first place – noting that what we’d like is some easily calculated ‘metric’ to identify these important

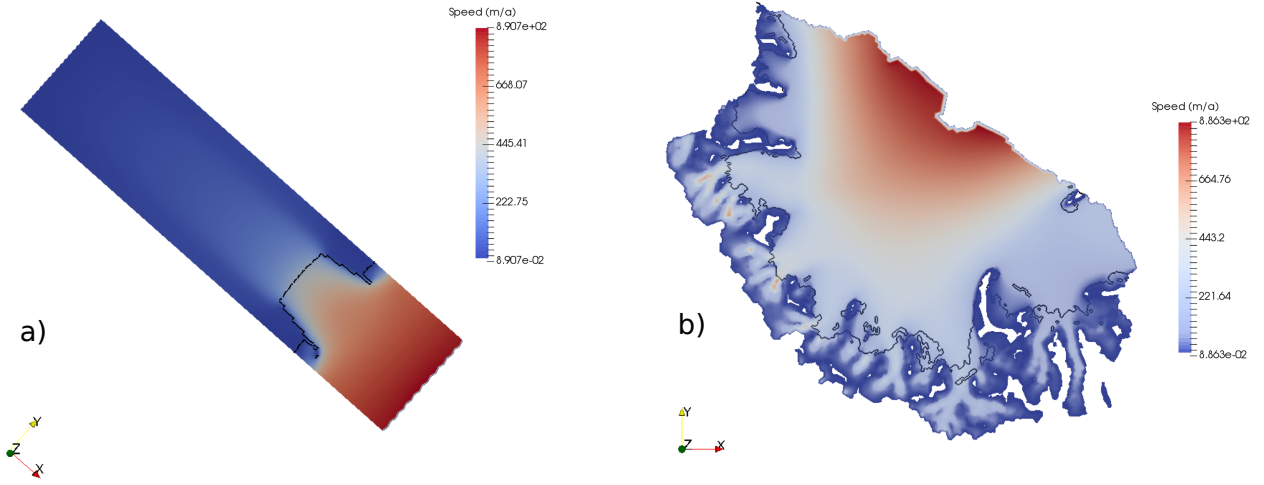


Figure 1. Plan view of steady-state surface speed for a) MISMIP+ and b) Larsen C Ice Shelf. The black curves show the grounding lines.

locations for us); 2) assess the ability of analogous, relatively easy to calculate, local buttressing metrics to indicate GLF sensitivity to local perturbations in ice shelf geometry; 3) point out where these metrics are useful and where (and why) they are not; 4) propose and demonstrate alternate, adjoint-based method that has advantages over previous methods.

Motivated by these studies, we build on and extend the methods and analysis of Fürst et al. (2016) and Reese et al. (2018) in order to make progress towards answering the following questions: (1) How do local and regional changes in ice shelf geometry affect distal changes in GLF? (2) Can we derive and define new analyses for understanding how observed or modeled spatial patterns in submarine melting influence GLF and, by extension, project how changes in submarine melt pattern and magnitude will impact GLF in the future?

Below, we first provide a brief description of the ice sheet model used in our study. We follow with a description of the model experiments. We then demonstrate and discuss the experimental results, including defining metrics for quantifying GLF sensitivity to changes in submarine melt, explaining their origins, and exploring their applicability and limitations. We conclude by proposing and demonstrating an adjoint-based calculation that provides a sensitivity map analogous to the perturbation experiments from Reese et al. (2018) but at the cost of a single adjoint solve in the model.

2 Model description

We use the MPAS-Albany Land Ice model (MALI; Hoffman et al., 2018), which solves the three-dimensional, first-order approximation to the Stokes momentum balance for ice flow¹. Using the notation of Perego et al. (2012) and Tezaur et al.

¹See Schoof and Hewitt (2013) for a full description of the Stokes momentum balance for ice flow and its lower-order approximations.

(2015a) this can be expressed as,

$$75 \quad \begin{cases} -\nabla \cdot (2\mu_e \dot{\epsilon}_1) + \rho_i g \frac{\partial s}{\partial x} = 0, \\ -\nabla \cdot (2\mu_e \dot{\epsilon}_2) + \rho_i g \frac{\partial s}{\partial y} = 0, \end{cases} \quad (1)$$

where x and y are the horizontal coordinate vectors in a Cartesian reference frame, $s(x, y)$ is the ice surface elevation, ρ_i represents the ice density, g the acceleration due to gravity, and $\dot{\epsilon}_{1,2}$ are the two dimensional strain rate vectors given by

$$\dot{\epsilon}_1 = \left(\begin{array}{c} 2\dot{\epsilon}_{xx} + \dot{\epsilon}_{yy}, \quad \dot{\epsilon}_{xy}, \quad \dot{\epsilon}_{xz} \end{array} \right)^T, \quad (2)$$

and

$$80 \quad \dot{\epsilon}_2 = \left(\begin{array}{c} \dot{\epsilon}_{xy}, \quad \dot{\epsilon}_{xx} + 2\dot{\epsilon}_{yy}, \quad \dot{\epsilon}_{yz} \end{array} \right)^T. \quad (3)$$

The “effective” ice viscosity, μ_e in (1), is given by

$$\mu_e = \gamma A^{-\frac{1}{n}} \dot{\epsilon}_e^{\frac{1-n}{n}}, \quad (4)$$

where γ is an ice stiffness factor, A is a temperature-dependent rate factor, $n = 3$ is the power-law exponent, and the effective strain rate, $\dot{\epsilon}_e$, is defined as

$$85 \quad \dot{\epsilon}_e \equiv (\dot{\epsilon}_{xx}^2 + \dot{\epsilon}_{yy}^2 + \dot{\epsilon}_{xx}\dot{\epsilon}_{yy} + \dot{\epsilon}_{xy}^2 + \dot{\epsilon}_{xz}^2 + \dot{\epsilon}_{yz}^2)^{\frac{1}{2}}. \quad (5)$$

Gradients in the horizontal velocity components, u and v , contribute to the individual strain rate terms in (5) and are given by

$$\begin{aligned} \dot{\epsilon}_{xx} &= \frac{\partial u}{\partial x}, \quad \dot{\epsilon}_{yy} = \frac{\partial v}{\partial y}, \quad \dot{\epsilon}_{xy} = \frac{1}{2} \left(\frac{\partial u}{\partial y} + \frac{\partial v}{\partial x} \right), \\ \dot{\epsilon}_{xz} &= \frac{1}{2} \frac{\partial u}{\partial z}, \text{ and } \dot{\epsilon}_{yz} = \frac{1}{2} \frac{\partial v}{\partial z}. \end{aligned} \quad (6)$$

A stress free upper surface is enforced through

$$90 \quad \dot{\epsilon}_1 \cdot \mathbf{n} = \dot{\epsilon}_2 \cdot \mathbf{n} = 0, \quad (7)$$

where \mathbf{n} is the outward pointing normal vector at the ice sheet upper surface, $z = s(x, y)$. The lower surface is allowed to slide according to the continuity of basal tractions,

$$2\mu_e \dot{\epsilon}_1 \cdot \mathbf{n} + \beta u = 0, \quad 2\mu_e \dot{\epsilon}_2 \cdot \mathbf{n} + \beta v = 0, \quad (8)$$

where β is a spatially variable friction coefficient, σ is the stress tensor and \mathbf{u} is the two-dimensional velocity vector (u, v) . On 95 lateral boundaries in contact with the ocean, the portion of the boundary above sea level is stress free while the portion below sea level feels the ocean hydrostatic pressure according to

$$2\mu_e \dot{\epsilon}_1 \cdot \mathbf{n} = \frac{1}{2} \rho_i g H \left(1 - \frac{\rho_i}{\rho_o} \right) \mathbf{n}_1, \quad 2\mu_e \dot{\epsilon}_2 \cdot \mathbf{n} = \frac{1}{2} \rho_i g H \left(1 - \frac{\rho_i}{\rho_o} \right) \mathbf{n}_2 \quad (9)$$

where \mathbf{n} the outward pointing normal vector to the lateral boundary (i.e., parallel to the (x, y) plane).

A more complete description of the MALI model, including the implementations for mass and energy conservation, can be
100 found in Hoffman et al. (2018). Additional details about the Albany momentum balance solver can be found in Tezaur et al.
(2015a, b).

Here, we apply MALI to experiments on both idealized and realistic marine-ice sheet geometries. For our idealized domain
and model state, we start from the equilibrium initial conditions for the MISMIP+ experiments, as described in Asay-Davis
et al. (2016). The model mesh is spatially uniform at 2 km resolution. For our realistic domain, we use Antarctica's Larsen C
105 Ice Shelf and its upstream catchment area. The model state is based on the optimization of the ice stiffness (γ in Eqn (4)) and
basal friction (β in Eqn (8)) coefficients in order to provide a best match between modeled and observed present-day velocities
(Rignot et al., 2014) using adjoint-based methods discussed in Perego et al. (2014) and Hoffman et al. (2018). The domain
geometry is based on Bedmap2 (Fretwell et al., 2013) and ice temperatures, which are held fixed for this study, are based on
Liefferinge and Pattyn (2013). Mesh resolution on the ice shelf is between 2 and 6 km and coarsens to 20 km in the ice sheet
110 interior. Following optimization to present-day velocities, the model is relaxed using a 100-year forward run, providing the
initial condition from which the Larsen C experiments are conducted (as discussed below). Both the MISMIP+ and Larsen C
experiments use 10 vertical layers that are finest near the bed and coarsen towards the surface. The grounding line position is
determined from hydrostatic equilibrium. A sub-element parameterization method is used to define basal friction coefficient
values at the grounding line (Seroussi et al., 2014) .

115 3 Perturbation experiments

To explore the sensitivity of changes in GLF to small, localized changes in ice shelf thickness, we conduct a number of
perturbation experiments analogous to those of Reese et al. (2018). Using diagnostic (instantaneous) model solutions, we first
study the instantaneous response of GLF for the idealized geometry and initial state provided by the MISMIP+ experiment
(Asay-Davis et al., 2016). We then conduct a similar study for Antarctica's Larsen C Ice Shelf using a realistic configuration
120 and initial state.

Our experiments are conducted in a manner similar to those of Reese et al. (2018). We perturb the coupled ice sheet-shelf
system by decreasing the ice thickness uniformly by 1 m over square grid "boxes" covering the base of the ice shelves, after
which we examine the instantaneous impact on kinematics and dynamics (discussed further below). For MISMIP+, we use a
uniform, hexagon-type, around 2-km mesh (for simplicity we use the term 2-km in the following). For the Larsen C Ice Shelf,
125 horizontal mesh resolution is spatially variable and we assign each grid cell to fall within one and only one box based on its
location. For MISMIP+, we perturb the thickness of the cell (hexagon) in the mesh. For Larsen C, we only use 20×20 km
square boxes (the same resolution as in Reese et al., 2018). Lastly, for the MISMIP+ 2-km experiments we note that, in order
to save on computing costs, we only perturb the region of the ice shelf for which $x < 530$ km (the area over which the ice shelf
is laterally buttressed). We also perturb only half of the ice shelf, $y > 40$ km, due to the symmetry about the center line, though
130 we analyze the response to these perturbations over the entire model domain.

Similarly to Reese et al. (2018), we define a GLF “response number”,

$$N_r = \left(\frac{R}{P} \right)^k, \quad (10)$$

where R is the ice flux change integrated along the entire grounding line, P is the mass change associated with a single grid-box perturbation and k is a power-law index that allows for the possibility of a nonlinear relationship between ice shelf buttressing and the change in GLF (see also Schoof, 2007). Here, we use $k = 1/n$ with $n = 3$.

Despite the existence of many possible factors linking GLF to ice shelf properties (ice flow direction, horizontal gradients in ice shelf geometry, stress fields, strain-rate fields, perturbation locations, etc.), here we mainly examine model stress fields and the distance between perturbation points and the GL. This is because, as we show below, these factors correlate closely with the sensitivity of changes in GLF to the imposed ice shelf perturbations. **SP: Maybe we can skip the previous sentences and just 140 skip to some form of the next one? We can motivate this simply by saying that the reason we use a buttressing number like Fürst et al is that it's a popular/standard and easy way to connect local ice shelf perturbations to the changes in GLF from the Reese experiments.** To incorporate the local stress field and its buttressing capacity into our analysis, we also calculate a “buttressing number”, N_b , analogous to that from Fürst et al. (2016),

$$N_b(\mathbf{n}) = 1 - \frac{\mathbf{n} \cdot \boldsymbol{\sigma} \cdot \mathbf{n}}{N_0}, \quad (11)$$

145 where N_0 is the vertically integrated ocean pressure ($N_0 = \frac{1}{2}(1 - \rho_i/\rho_w)gH$) and ρ_i (910 kg m^{-3}) and ρ_w (1028 kg m^{-3}) are the density of ice and ocean water, respectively. $\sigma_{nn} = \mathbf{n} \cdot \boldsymbol{\sigma} \cdot \mathbf{n}$ is the normal stress along a specified horizontal direction given by the normal vector \mathbf{n} (see details in below).

4 Results and Discussion

4.1 Correlation between buttressing and changes in GLF

150 A decrease in ice shelf buttressing tends to lead to an increase in GLF (e.g., Gagliardini et al., 2010) and intuitively we expect that the GLF should be relatively more sensitive to melt changes that occur in regions of relatively larger buttressing. Here, we aim to better understand and quantify the relationship between the local ice shelf buttressing “strength” (given by N_b) and changes in GLF (given by N_r). Can the change in GLF for a given melt perturbation be quantified (in the predictive sense) as a function of the buttressing number? In Fig. 2, we show correlations between N_b and N_r for perturbations applied to the 155 MISMIP+ domain when N_b from (11) is defined based on the direction of the first principal stress (σ_{p1})². In Fig. 2b, we include all perturbed ice shelf locations in the comparison and find relatively weak $N_b:N_r$ correlations. In Fig. 2c, we remove from the comparison points that are 1) weakly buttressed ($x > 480 \text{ km}$, where the ice shelf becomes unconfined) and 2) within 10 km of the GL, and a much stronger $N_b:N_r$ correlation emerges. In Fig. 2d, we plot the $N_b:N_r$ correlation for locations where $x > 480 \text{ km}$ and the magnitude of the thickness gradient $|\nabla H| < 7 \times 10^{-3}$ (a similar plot with the buttressing number

²We expand on our reasons for choosing σ_{p1} below.

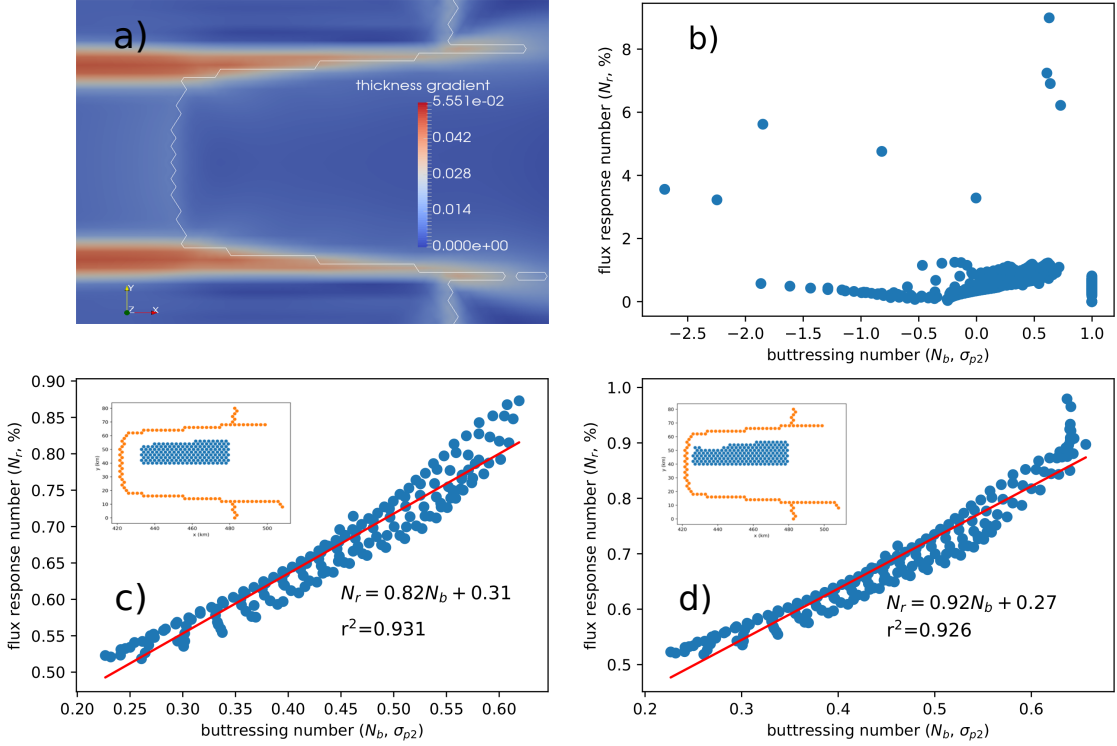


Figure 2. (a) MISMIP+ steady-state geometry. Color represents the magnitude of the ice thickness gradient and the white line represents the GL. (b) $N_b:N_r$ correlation for all perturbation points. (c) $N_b:N_r$ correlation for perturbation points within the confined region of the shelf ($x > 480$) and >10 km from the GL; (d) $N_b:N_r$ correlation for perturbation points within the confined region of the shelf and with a thickness gradient magnitude $|\nabla H| < 7 \times 10^{-3}$. In (c) and (d), the orange dots in the insets represent the GL grid cells, and the blue dots the perturbation grid cells. SP: Matt suggested expanding this to include 2 more panels using the points in (d) – the flow direction and the p_2 direction (the goal being to show that the correlations are pretty bad). Then we could also add another panel along the bottom which is the ‘continuous’ version of these (i.e., the red curve in Fig. 3a).

160 defined based on the direction of the second principal stress is shown in Fig. A1). The strong similarities between Figures 2c and 2d suggest that the seemingly *ad hoc* “distance from the grounding line” constraint is important for removing areas of complex geometry (and hence complex dynamics) from the $N_b:N_r$ comparisons. We discuss possible reasons for this further below.

4.2 Directional dependence of buttressing

165 The buttressing number, N_b , is computed using the normal stress (σ_{nn}) projected onto a specific direction, see Equation (11). Therefore, the buttressing number at any perturbation point varies depending on the chosen direction. Fürst et al. (2016) calculated N_b along two directions, the ice flow direction (\mathbf{n}_f) and the direction corresponding to the second principal stress (σ_{p2}) (\mathbf{n}_{p2}). They found that the latter—the direction corresponding to the maximum compressive stress (or the least extensional stress)—best identified “passive” regions, where the ice shelf provides little or no buttressing. In Fig. 3, we plot the correlation 170 coefficients (r^2) between N_r and N_b where the direction corresponding to σ_{nn} varies continuously between 0 and 180° (as a function of the angle $\Delta\phi$) relative to the direction corresponding to the first principle stress (σ_{p1}) (\mathbf{n}_{p1}). We find the largest correlation coefficient ($r^2 > 0.9$) when N_b is aligned with \mathbf{n}_{p1} ($\Delta\phi = 0^\circ$) and the smallest correlation coefficient ($r^2 < 0.4$) when N_b is aligned with \mathbf{n}_{p2} ($\Delta\phi = 90^\circ$). We can also see the corresponding variations in buttressing number N_b in Fig. A2, where the maximum buttressing number is calculated from $N_r(\mathbf{n}_{p2})$ according to Equation (11).

175 A similar conclusion can be reached when the buttressing number is calculated by projecting σ_{nn} onto \mathbf{n}_f ³. In Fig. 3a, the blue line shows the $N_b:N_r$ correlation for the case of rotating relative to \mathbf{n}_f . For around 50% of the perturbation points, the angles of flow directions are $30\text{--}50^\circ$ ($\Delta\varphi$) more than that of the directions of first principle stresses (from Fig. 3b), which is consistent with the phase difference between the blue and red curves in Fig. 3a. For example, for the \mathbf{n}_f curve (blue), we have the smallest value at $\Delta\phi \approx 38^\circ$, i.e., 38° relative to the flow direction. Since the angles of \mathbf{n}_f are $30\text{--}50^\circ$ more than that of \mathbf{n}_{p1} , the lowest value should occur at $68\text{--}88^\circ$ ($\Delta\phi + \Delta\varphi$) relative to \mathbf{n}_{p1} , which is corresponding to \mathbf{n}_{p2} . This is in consistent 180 with the position of the smallest value for the σ_{p1} direction curve (red; $\Delta\phi \approx 90^\circ$).

Based on the discussion above and the work of Fürst et al. (2016), it appears that $N_b(\mathbf{n}_{p2})$ provides a good indicator for the maximum buttressing at any location on the shelf and for identifying passive ice shelf areas. Yet it may not be a good metric for quantifying the sensitivity of GLF response to sub-shelf basal melt perturbations. In the following sections, we explain how 185 and why changes in GLF are sensitive to the choice of direction when calculating the ice shelf buttressing number.

4.3 Velocity changes in the vicinity of perturbation points

The correlation between changes in GLF and normal stress (buttressing) directions can be partly understood by examining the spatial patterns of velocity change associated with thickness perturbations. In Fig. 4, we plot histograms of the maximum 190 (red) and minimum (blue) speed changes around each perturbation point as a function of angular distance relative to \mathbf{n}_{p1} ($\Delta\phi$, as in Fig. 3a). That is, we count the number of neighboring cells that have maximum (most increased or least decreased) and minimum (most decreased or least increased) speed changes (for each cell, there is only one neighbor with maximum or minimum speed change). The maximum speed changes cluster within $0 of \mathbf{n}_{p1} and the minimum speed changes cluster within $60, indicating that the majority of speed increases in the immediate region of a perturbation are more closely aligned with \mathbf{n}_{p1} (and likewise, the majority of velocity decreases are more closely aligned with \mathbf{n}_{p2}). This finding supports$$

³In Fürst et al. (2016), the ice flow direction is the second direction considered when calculating the local ice shelf buttressing number (with the first direction considered being \mathbf{n}_{p2}).

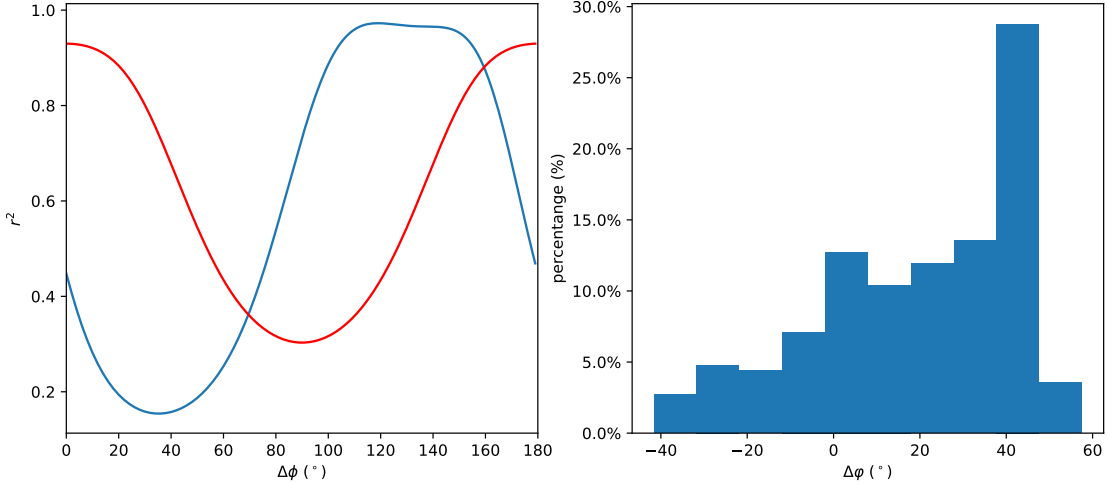


Figure 3. (a) $N_b:N_r$ correlation coefficients for σ_{nn} values rotated counterclockwise by $\Delta\phi$ degrees relative to \mathbf{n}_{p1} (red) and \mathbf{n}_f (blue). (b) Histogram of the angular differences between \mathbf{n}_f and \mathbf{n}_{p1} . The perturbation points analyzed here are those shown in the inset of Fig. 2d. **SP:** Matt/Xylar suggested breaking the velocity part of this fig out into its own fig.

195 the hypothesis that the thickness perturbations induce velocity increases along favored directions and that, for the MISMIP+ domain, \mathbf{n}_{p1} is favored. **SP:** I think it would help if we try to connect this more clearly to the next section. That is, here we show that a local perturbation leads to speed increases along preferred directions. Below, we show that local perturbations lead to similar speed increases (also along preferred directions) but at the GL.

4.4 Speed and stress changes along the GL

200 Further insight into the importance of \mathbf{n}_{p1} is given by examining changes in the state of stress and velocity as a result of a perturbation in local ice thickness. To this end, we define the metric Υ ,

$$\Upsilon = \text{Corr} \left(\frac{\sigma_p - \sigma_c}{\sigma_c}, \frac{u_p - u_c}{u_c} \right), \quad (12)$$

SP: need to update this equation to clarify the following things: 1) epsilon is scalar function of x,y (that is, we calculate a single value of it for each perturbation point on the ice shelf), 2) the two terms in parentheses are vectors of points along the GL, 3) the operation here is a dot product, so that the vectors collapse to a scalar value, which is what is evaluated. where the subscripts p and c denote the perturbation experiments and the “control” (i.e., the initial condition), respectively, and σ and u denote the stress component and ice speed along the GL, respectively. Υ , a correlation coefficient, is a measure of the consistency between the magnitude and sign of the change in the model stress and velocity states along the GL between the control and perturbation experiments. We calculate Υ for every perturbation point and for all directions in the span of $\Delta\phi = 0-180^\circ$ relative to \mathbf{n}_{p1} (Fig. 5). For normal stress perturbations relatively more parallel to \mathbf{n}_{p1} (closer to 0° or 180°),

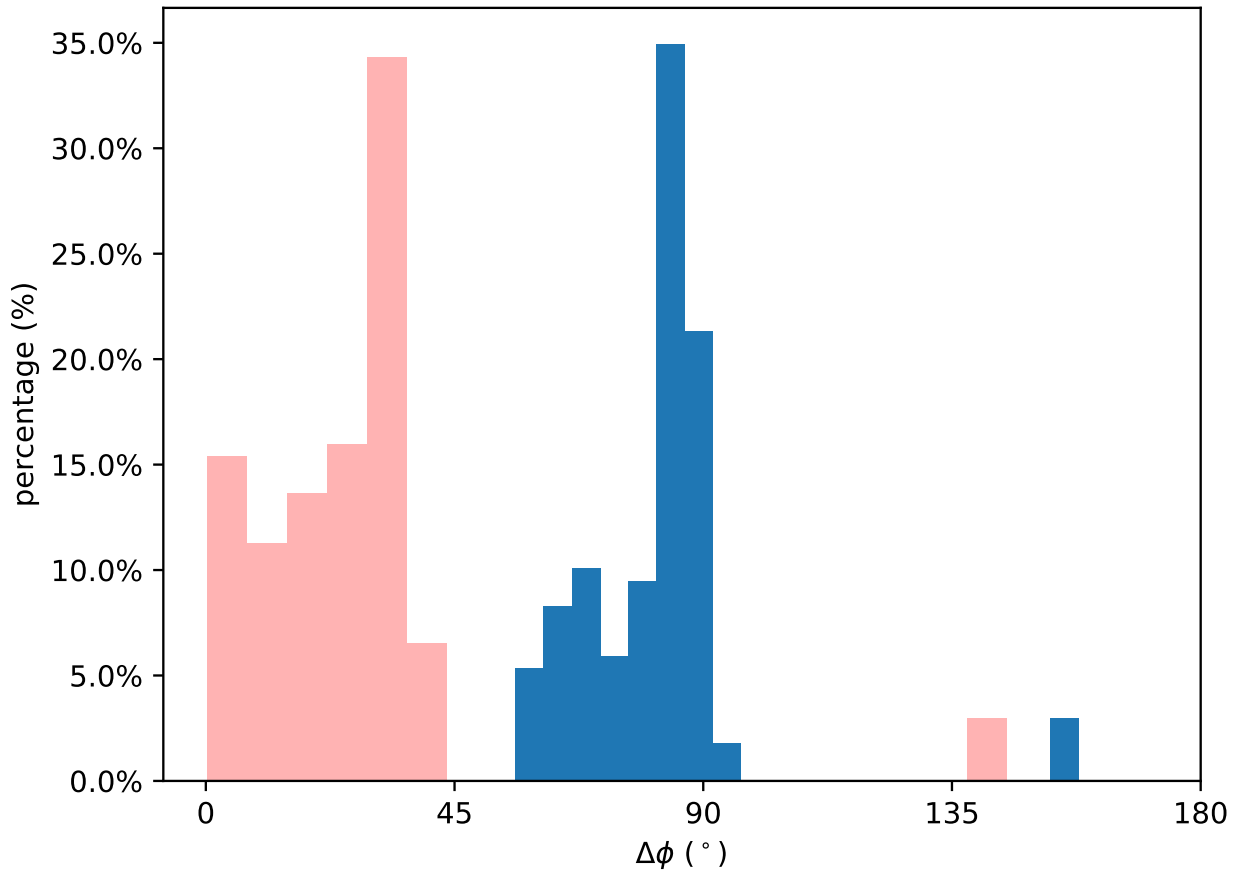


Figure 4. Histograms for the maximum (red) and minimum (blue) percent speed change in grid cells adjacent to a thickness perturbation point, plotted as a function of angular distance with respect to the σ_{p1} direction. Points analyzed are those from Fig. 2d.

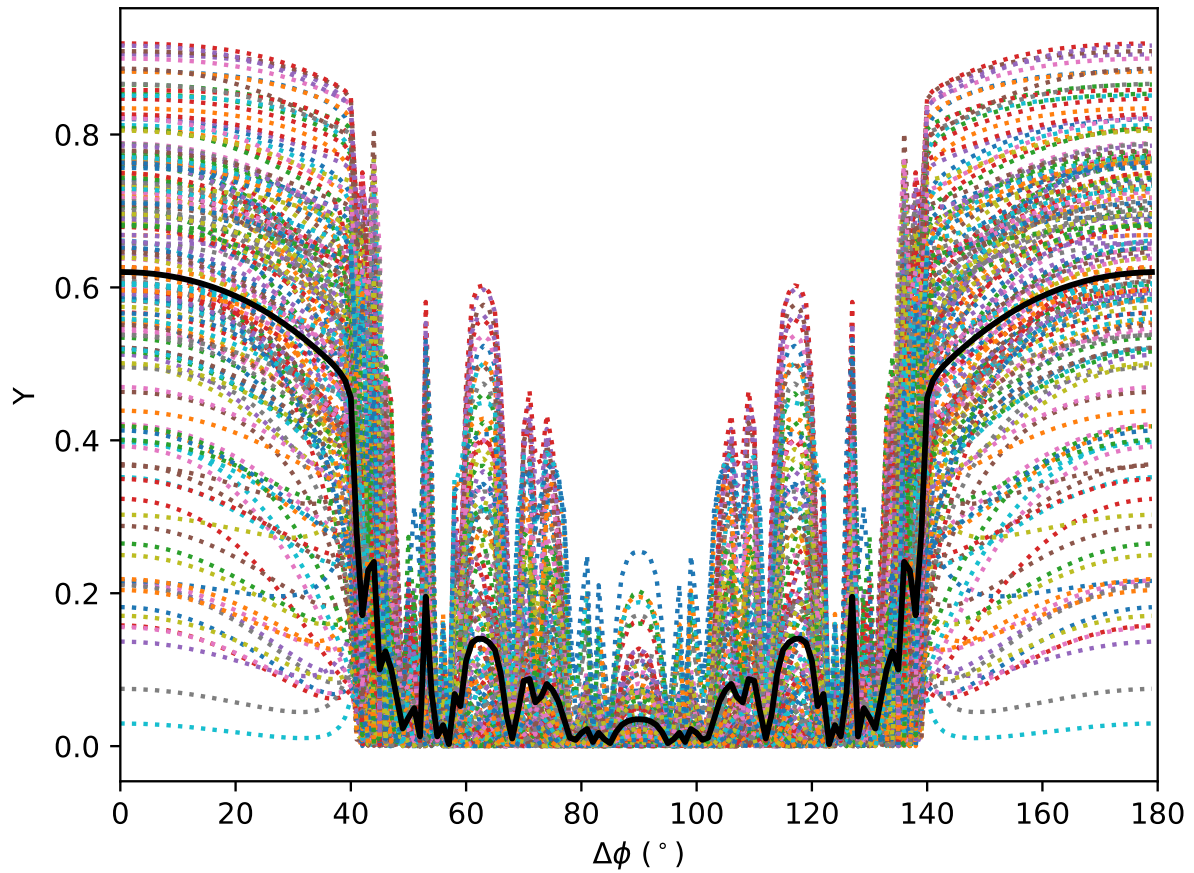


Figure 5. Correlation between the change in normal stress and the change in ice surface speed along the GL (i.e., Υ from (12)). The horizontal axis shows how Υ varies as a function of the direction of the normal stress, rotated counterclockwise from \mathbf{n}_{p1} . Colored, dotted curves each represent a single perturbation experiment and the thick black curve is their mean for a given value of $\Delta\phi$. **SP: We should swap the order of this figure with the next one, since this is the 'continuous' version of that one (see related note in caption below).**

there is a much stronger correlation between changes in normal stress and changes in ice surface speed (and hence the ice flux) than for normal stress perturbations that are relatively more parallel to \mathbf{n}_{p2} (closer to 90°). By plotting spatial maps of Υ for every perturbation point of interest in the domain, we show that there is generally a stronger correlation, in general, between changes in normal stress and velocity along \mathbf{n}_{p1} (Fig. 6a) than along \mathbf{n}_{p2} (Fig. 6b). If we plot the change in N_b between the perturbation and control experiments at every point for $N_b(\mathbf{n}_{p1})$ (Fig. 7a) and for $N_b(\mathbf{n}_{p2})$ (Fig. 7b), we see that the reduction in buttressing is generally larger in magnitude, more spatially extensive, and more aligned with the mean ice flow direction

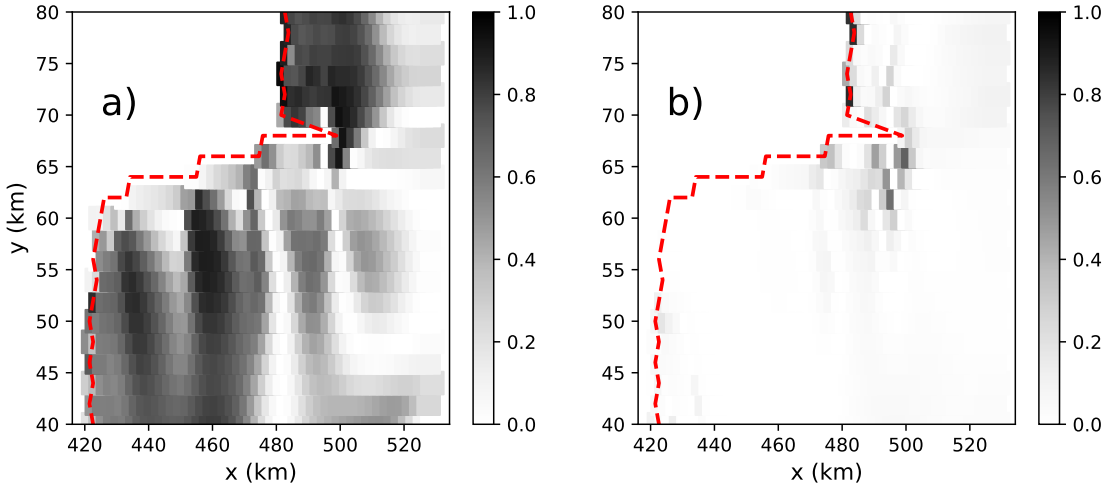


Figure 6. Spatial maps of the correlation coefficient Υ from Equation (12) over the MISMIP+ domain for normal stress changes calculated parallel to (a) \mathbf{n}_{p1} and (b) σ_{p2} . Note that Υ is a metric for the changes of stress and speed along GL. **SP: Swap the order of this fig w/ the one above, since this shows what Upsilon looks like along only two directions (while that figure shows the 'continuous' form of Upsilon).**

(left to right in Fig. 7) for the case of $N_b(\mathbf{n}_{p1})$ (Fig. A4 shows a detailed comparison between the change in stress and velocity along the GL for a single perturbation on the ice shelf).

One possible reason that we might see such direction-dependent correlations might be due to the way perturbations propagate through ice shelves. The energy of from a perturbation propagates with the group velocity, which can be analyzed using a Fourier transform, similarly to Gudmundsson (2003). Using simplified geometry, Gudmundsson (2003) analyzed the propagation of basal perturbation to glacier surface and found that the direction of group velocity is aligned closely with the main flow. The existence of a preferred propagation direction for the perturbations can possibly lead to our findings that favor the first principal stress directions. **SP: At the end of this section, it would be useful to summarize what these two sections (and figs 4, 5, 6) tell us. That is, that one possible explanation for the strong correlation between GLF changes and buttressing calculated in the p1 direction is that local perturbations in thickness trigger velocity increases along favored directions. And, for both local and distal (at the GL) increases in velocity, those favored directions are also aligned with the p1 direction. We might think about more clearly joining these two sections into a single chunk of discussion by putting the 'velocity changes in the vicinity of ...' and 'speed and stress changes ...' sections above under a single broader section, called something like 'Directional dependence of changes in velocity' (which then jibes a bit better with the title of the section above).**

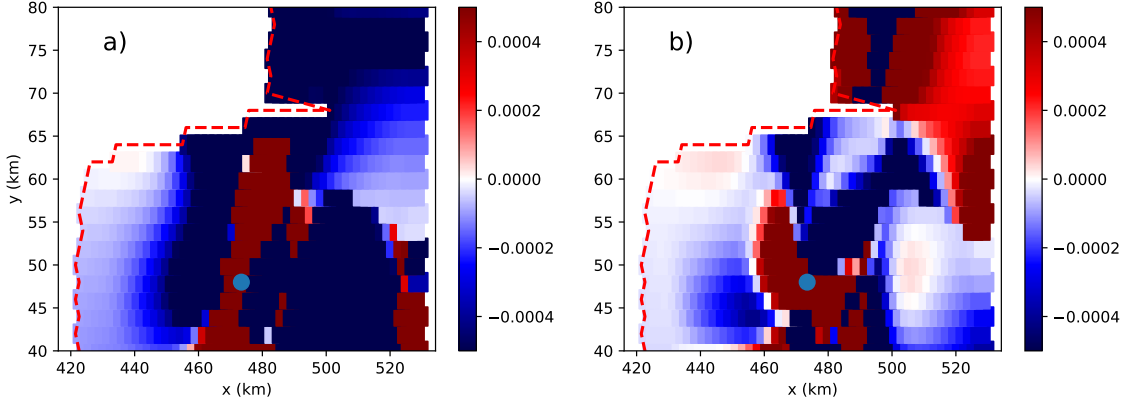


Figure 7. The percentage changes of buttressing number across the MISMIP+ (half) domain under the perturbation shown as the blue circle. In a) and b), the buttressing numbers are calculated along n_{p1} and n_{p2} , respectively.

4.5 A metric connecting perturbations in thickness to changes in GLF

SP: I think we might want to copy/paste this whole section into the appendix for the time being. In some of the discussion with Xylar and Matt, we decided this does not necessarily add any new information that we don't already know from other calculations above (e.g., it uses/needs a lot of the same information that we currently show in fig 3 above) but it is much harder to understand. At this point, I think we know we aren't going to find a better simple metric than just the buttressing number using the p1 direction, so it doesn't make sense to try to introduce a more complicated one (and we're going to advocate for the adjoint approach in the end anyway). The change in GLF for a given perturbation to the ice-shelf thickness must be controlled by both the perturbation itself (the local change to the geometry, stress, and velocity fields) and the broader, surrounding ice dynamical setting (the regional geometry, stress, and velocity fields). To explore this further, we propose the following simplified metric, which connects and combines local aspects of a perturbation with its regional impact on GLF:

$$\Lambda = \sum_i^I \frac{1}{d_i} |\cos(\theta_i)|, \quad (13)$$

where I is the total number of grid cells along the GL, d_i is the distance between the perturbation point and the i -th GL grid cell, and θ_i is the angular difference between the direction of the specified normal stress (e.g., σ_{p1}) at the perturbation point and the flow direction for the i -th GL grid cell. The metric Λ thus aims to capture two important factors impacting changes in GLF as a function of perturbations in ice shelf thickness: 1) the distance between the perturbation point and the GL (intuitively, the closer the perturbation to the GL, the larger the impact—also see the related discussion in the next section). We note that, while this metric does not *explicitly* account for kinematic or dynamical processes (i.e., there are no terms explicitly involving

250 velocities or stresses), it accounts for them *implicitly* through the term in the numerator, which requires knowledge of the velocity and stress directions.

Similar to above, we rotate the buttressing direction by 0–180° with respect to \mathbf{n}_{p1} , and calculate Λ for each perturbation point. From Fig. 8 we can see that Λ has large values when the buttressing directions are close to \mathbf{n}_{p1} ($\Delta\phi = 0^\circ$ or $\Delta\phi = 180^\circ$). A possible reason is that, for the MISMIP+ geometry, the velocity across the GL (and thus the GLF) is largely parallel with the 255 σ_{p1} direction at the GL (see Fig. A3). This, in turn, is largely the result of extensional flow across the majority of the MISMIP+ GL. For real ice shelves, where the pattern of ice flow across the GL is generally more complex (e.g., in the presence of an ice rise downstream from the GL), we expect a metric based on the assumption that σ_{p1} and changes in GLF are well correlated to be less robust .

4.6 Application to Larsen C Ice Shelf

260 To explore whether the $N_b:N_r$ correlations found for the MISMIP+ test case hold for realistic ice shelves, we apply a similar analysis to our Larsen C domain. In this case, the computational mesh resolution varies, from finer near the GL (2 km) to coarser towards the center of the ice shelf and calving front (6 km). In order to be comparable to the experiments and results of Reese et al. (2018), we use 20 km × 20 km boxes for the application of ice-thickness perturbations, where the number of grid cells contained within each perturbation “box” is adjusted to sum to their correct total area. Additionally, to investigate 265 the impacts of the complex geometry of the Larsen C Ice Shelf (i.e., the GL shape, the existence of ice rises, etc.), we apply two sets of perturbation experiments for which the 20 km × 20 km averaging boxes both do and do not include perturbations applied to cells near the GL.

Analogous to Figures 3a,b for the MISMIP+ test case, Figures 9a,b shows the $N_b:N_r$ correlations for the Larsen C model 270 domain (including only perturbation points that are >50 km away from both the calving front and the GL). As previously, calculating N_b using $\sigma_{nn}=\sigma_{p1}$ provides the best overall correlation between N_b and N_r (red curve for $\Delta\phi = 0^\circ$) and calculating N_b using $\sigma_{nn}=\sigma_{p2}$ provides the worst overall correlation (red curve for $\Delta\phi = 90^\circ$). The phase difference between the σ_{p1} and flow direction results can also be partially explained by their respective angle differences. In Fig. 9b we can find the local flow direction is typically oriented around 90–100 degrees counterclockwise of the local σ_{p1} direction. This is a bit biased than the around 70 degree difference in Fig. 9a. However, considering the stress values (and thus N_b) for each perturbation box are 275 averaged over multiple cells, we argue this difference is probably an acceptable error during our calculation. **SP: As noted above, I'm not sure about introducing the discussion about results relative to the velocity direction, as I think they are maybe just confusing. So leaving this part of the text alone for now. TZ: Personally I prefer to let the flow direction curve remain. I think this may give the reader more confidence of our results. I'll also wait Matt and Xylar's opinions about this.**

In Figures 9c,d we redo the same analysis but include points near the GL (more than 10 km away from the calving front 280 with a thickness gradient $|\nabla H| < 2 \times 10^{-3}$). This reduces the r^2 values by a factor of two and also changes the relationship between the correlation coefficient and the alignment relative to σ_{p1} . Specifically, while the direction aligned with σ_{p2} still gives the worst $N_b:N_r$ correlation, the direction giving the best correlation is rotated by approximately 40° relative the direction associated with σ_{p1} . This indicates that thickness perturbations at these locations are propagating, at least in part, along both

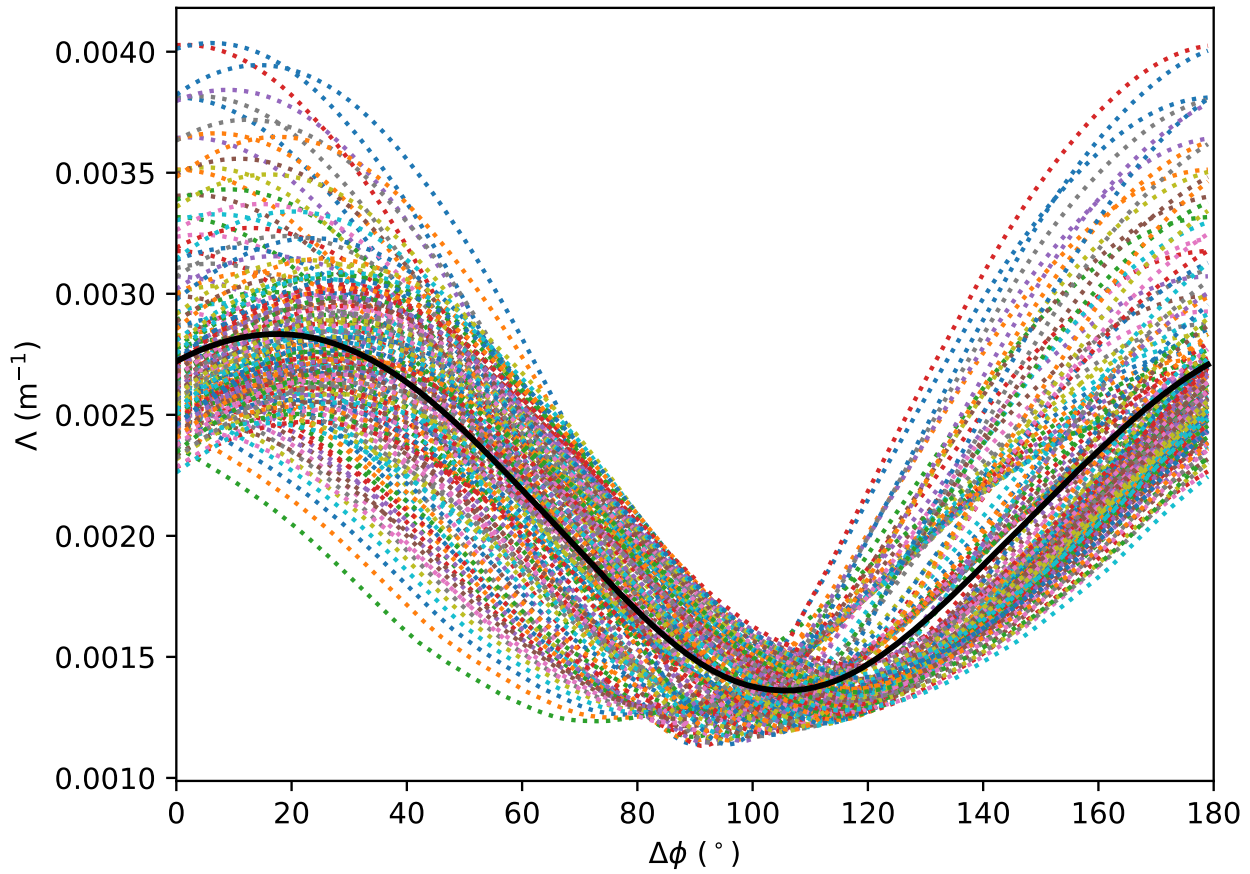


Figure 8. A metric that gives a possible explanation of the connection between perturbation and GLF. Same as above, $\Delta\phi$ is the angular distance from the direction of σ_{p1} . The line types are the same as in Fig. 5

the σ_{p1} and σ_{p2} directions and leading to increases in GLF. In addition, there is no clear relationships between changes of
285 velocity and specified normal stresses along the GL for Larsen C Ice Shelf (Fig. A5), as their is for the MISMIP+ domain (3),
due to the complex geometry and ice flow along the GL **TZ: A thought: I am not sure if it can get better if we pick some**
of the cells with simpler geometry on GL.. SP: I'm not really sure what else we can say about this, other than that it's an
indication that using σ_{p1} and σ_{p2} in the calculation of N_b is probably just more problematic for complex geometries. I think
it's fair to leave it at that in this paragraph, since overall, we know that the main conclusions are going to be that this type of
290 analysis appears to be of limited use on realistic geometries for a few different reasons.

4.7 The impact of perturbations applied near the GL

For thickness perturbations applied near the Larsen C GL, the correlations between buttressing number and changes in GLF
discussed above (e.g., Figs. 2, 3) do not obviously hold. This may be due to an additional dependence on the distance between
the GL and perturbation locations or on particular, nearby geometric features. While a perturbation decays over distance (Lick,
295 1970), cells at the GL that are near to a perturbation location will be impacted by that perturbation relatively easily. This can
be verified by looking at the standard deviations of GL velocity change due to each perturbation (Fig. 10). For a perturbation
applied close to the GL, the corresponding GLF change is, in general, confined to a local region near that perturbation. On the
other hand, the impact on the GLF in areas far from that local region are small (resulting in large standard deviations; also see
Fig. A6). A practical implication of this finding is that strong spatial heterogeneity in GL retreat could result from ice shelf
300 thickness perturbations (e.g., submarine melting) applied very close to the GL.

The propagation of perturbations is also strongly impacted by the geometry of the GL. For example, in the MISMIP+ test
case the perturbations near $480 < x < 500$ km and $y = 65$ km in Fig. 10a cannot impact the ice flow on the other side of the
grounded peninsula, at $480 < x < 500$ km and $70 < y < 80$ km (see also Fig. A7a). For a perturbation within a local embayment
305 of the Larsen C Ice Shelf, the embayment itself “shades” the majority of the rest of the Larsen C GL from the impacts of the
perturbation (Fig. A7b). This is one of the primary factors complicating the use of the buttressing number as a practical metric
for diagnosing GLF sensitivity on real ice shelves.

4.8 Adjoint sensitivity

Motivated by some of the complications discussed above when looking for a simple metric for diagnosing GLF sensitivity
to local ice shelf thickness changes, we now investigate a different approach. This approach provides a sensitivity map of
310 the GLF analogous to the one proposed and discussed above but associated to infinitesimal rather than finite perturbations.
Instead of computing the GLF change due to individual perturbations at each n model grid cells, requiring n forward solves,
the adjoint method allows to compute the sensitivity at all cells simultaneously at the cost of a single linear solve. Briefly, this
method involves the solution of an auxiliary linear system (the adjoint system) to compute the so-called Lagrange multiplier
315 (a variable that has the same dimension of the velocity solution). The matrix associated to the system is the transpose of the
Jacobian of the first-order flow model. In addition, the adjoint method requires the computation of the partial derivatives of
the FO residual and the GLF w.r.t. the velocity solution and the ice thickness. We compute the Jacobian and all the other

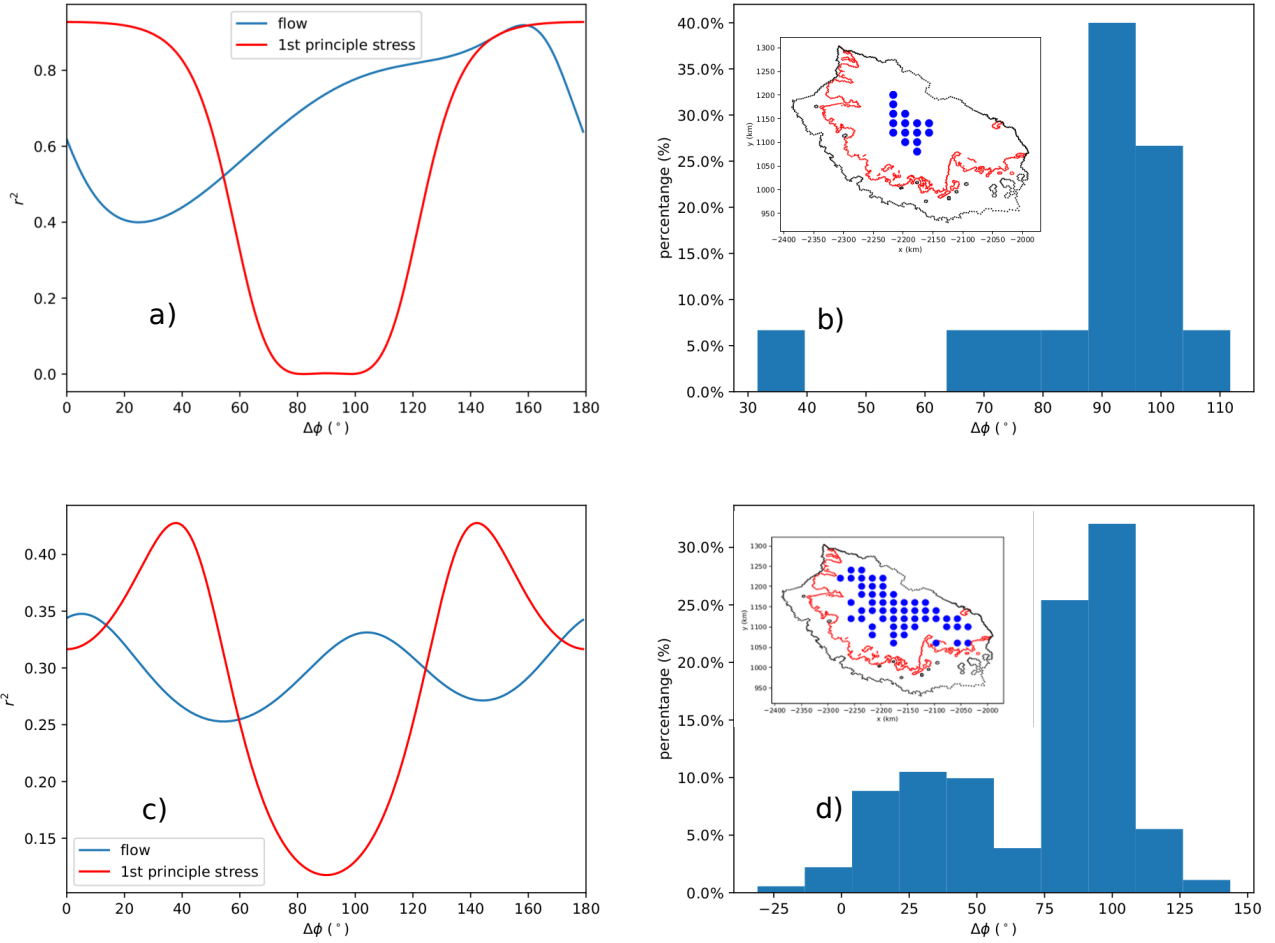


Figure 9. (a, c) The $N_b:N_r$ correlation coefficients for each direction rotated counterclockwise from the σ_{p1} (red) and flow direction (blue). (b, d) The histogram of the angular differences between the ice flow and σ_{p1} directions. The insets in b) and d) show the locations of the 20 km \times 20 km perturbation boxes (blue circles). **SP: We could make this plot simpler/smaller by removing the vel correlations and histograms and just including the red lines and the maps. Especially if we don't think the flow direction based metric is useful and we don't spend anytime talking about it.**

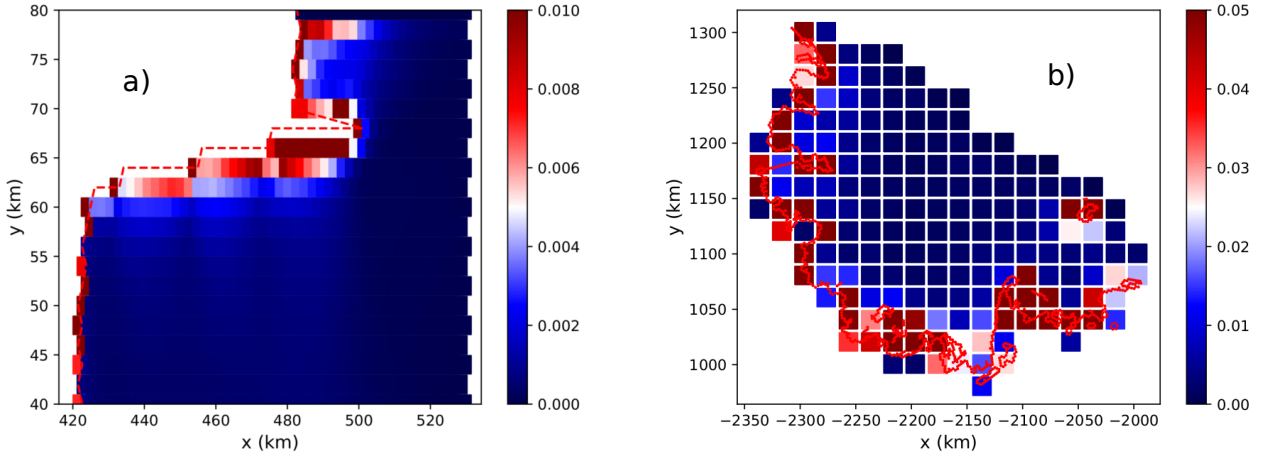


Figure 10. Standard deviation of velocity change along GL for each perturbation point for the MISMIP+ (a) and Larsen C (b) experiment. The red dashed lines (points) are the GLs for MISMIP+ (a) and Larsen C (b).

derivatives using automatic differentiation. We note that the computation of the derivatives require special attention because a change in the thickness affects the geometry of the problem, and so shape derivatives need to be taken into account as well. A similar adjoint approach has been proposed in Goldberg et al. (2019) to compute the sensitivity of the volume above flotation w.r.t the melting rate averaged over the period 2011–2015. In contrast to our approach, the authors have to compute *transient* sensitivities because their quantity of interest is averaged over a period of time.

In Fig. 11, we provide a demonstration of this method for the case of the MISMIP+ domain by comparing sensitivities deduced from 730 individual forward model evaluations (i.e., the perturbation experiments discussed above, which are analogous to those in Reese et al. (2018)) with those deduced from a single model adjoint solve. Here, the “sensitivity” is defined as ...
325 *SP: need more details from Mauro here.*

The comparison in Fig. 11 demonstrates that, for points in the domain we expect to be comparable, the two approaches provide a near exact match. The two methods disagree in regions very near to the GL (see Fig. A8), which we hypothesize to be the result of nonlinearities near the GL that prevent accurate use of the tangent linear model for deducing sensitivities. This method provides clear advantages over the more *ad hoc* analysis methods discussed above in that, in addition to providing a map of where the GLF is most sensitive to local ice thickness changes, the impact of those thickness changes on GLF flux can be calculated directly from the value of the sensitivity. *SP: I wonder if we also want to show a map of those sensitivities (with units) in the appendix somewhere.*

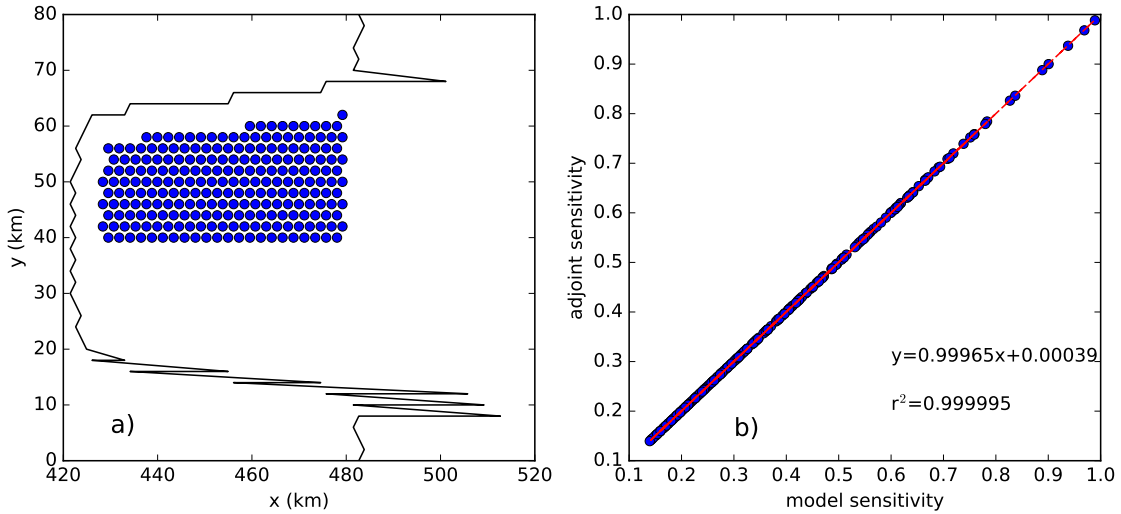


Figure 11. Grounding line flux sensitivity for the MISMIP+ domain calculated from individual perturbation experiments versus derived from a model adjoint (perturbation locations are shown by circles in a). Perturbation-experiment (x-axis) and adjoint-derived (y-axis) sensitivities (see text for definition) are plotted against one another in b). In a and b, the red circles indicate near-GL (<2 km) perturbation points, which are omitted in the comparison in b and d. The GL in a and c is shown by the black curve. In b and d, the red line is a linear regression between the perturbation-experiment and adjoint-derived sensitivities.

5 Conclusions

There has been much recent and intense interest in the marine ice sheet instability (MISI), primarily in the context of the
 335 potential ongoing and future unstable retreat of sectors of the West Antarctic ice sheet (add REFS?). Due to the connections
 between ice shelf buttressing and the MISI, attention has shifted to better understanding the sensitivity of GLF to ice shelf
 basal melting. Specifically, where are ice shelves most vulnerable to basal melting in the context of increased GLF and can we
 predict the sensitivity of changes in GLF to ice shelf melting based on the present-day geometry and flow field of the ice shelf?
 In this study, we have attempted to address these questions, with the following findings:

340 The GLF response to thickness perturbation is highly dependent on the direction of buttressing. Although, locally, the
 buttressing is maximum along the second principal stress (σ_{p2} direction, we find a much better correlation between GLF
 response to the buttressing defined in terms of the first principal stress (σ_{p1}) at perturbation points that are located near the
 center region of the ice shelf. The buttressing number (along \mathbf{n}_{p2} and \mathbf{n}_f) approach adopted in Fürst et al. (2016) for identifying
 345 passive ice regions doesn't properly apply in terms of finding sensitive ice shelf regions that well connect basal melting and
 GLF responses.*SP: We can hit this a little bit harder by pointing out that this is in disagreement with the work of Furst et
 al., who use sigma p2 to identify regions of passive ice. Tong: I add a sentence here* We argue that this is because the GLF
 response is controlled by both the dynamics at GL and the perturbation points and their relationship (for example, (13)) in

between. Therefore, we cannot easily predict GLF response by only analyzing the geometric and dynamic features of a local perturbation, i.e, large basal melting at a location of high buttressing (large buttressing number along the σ_{p2} direction) do not
350 always lead to large GLF increases.

Near the GL, there is no clear connection between the buttressing at the perturbation points and the response of GLF, as
1) the pattern of ice flow across GL may be highly heterogeneous in space for real ice shelves and 2) the propagation of
perturbation will be strongly affected by the local GL geometry. In this case, the distance between the perturbation point and
GL may be playing the critical role, as the energy of the perturbation decays over distance. We observe large increase of ice
355 speed and flux for GL cells that are close to the perturbation points. This indicates two possible consequences: 1) the grounded
ice sheet dynamics will be negligibly affected if the GL dynamics is insensitive to melt perturbation (e.g., the bed topography
is downward sloping or the ice thickness at GL is thin); 2) the retreats of GL will be spatially heterogeneous if the dynamics
of local GL is sensitive to the perturbation (e.g., the bed topography has retrograde slope and large ice thickness) while the
remote portion of GL experience relatively little impact from the perturbation.

360 Considering the complex pattern of the connection between GLF response and buttressing number at perturbation points for
real ice shelves, we propose to adopt the adjoint sensitivity method in the ice sheet model to accurately capture the dynamic
change of GLF sensitivities. For perturbation points that are near to the (can we say something quantitative here, like using the
thickness gradient metric?) GL, the adjoint method may not provide consistent results due to the large gradient of ice geometry
365 (nonlinearity), but it can capture the complex ice dynamics along GL for real ice shelves for most perturbation points. By
introducing the adjoint sensitivity method we do not need to do every perturbation experiment to determine the sensitivity map
of an ice shelf. **TZ: I think we need further evidence of adjoint ability on complex real ice shelves. What do you think,**
Steve? SP: I'm inclined to see if we can get away with it for now, and only address it if we are asked for it in review.

For ice-sheet models that lack an adjoint capability, our analysis here can also provide a rough guide to determine the
sensitivity of GLF to basal melt at different locations on the ice shelf (e.g. use a metric like (13) to find the dominant buttressing
370 direction and compare the buttressing number values at different perturbation points). But we acknowledge that it is a somewhat
arbitrary choice to remove those perturbation points that are near GL and calving front.

6 Acknowledgements

Support for this work was provided through the Scientific Discovery through Advanced Computing (SciDAC) program funded
by the US Department of Energy (DOE), Office of Science, Biological and Environmental Research, and Advanced Scientific
375 Computing Research programs. This research used resources of the National Energy Research Scientific Computing Center,
a DOE Office of Science user facility supported by the Office of Science of the US Department of Energy under contract no.
DE-AC02-05CH11231.

References

- Asay-Davis, X. S., Cornford, S. L., Durand, G., Galton-Fenzi, B. K., Gladstone, R. M., Gudmundsson, H., Hattermann, T., Holland, D. M.,
380 Holland, D., Holland, P. R., et al.: Experimental design for three interrelated marine ice sheet and ocean model intercomparison projects: MISMIP v. 3 (MISMIP+), ISOMIP v. 2 (ISOMIP+) and MISOMIP v. 1 (MISOMIP1), *Geoscientific Model Development*, 9, 2471–2497, 2016.
- Barletta, V. R., Bevis, M., Smith, B. E., Wilson, T., Brown, A., Bordoni, A., Willis, M., Khan, S. A., Rovira-Navarro, M., Dalziel, I., et al.: Observed rapid bedrock uplift in Amundsen Sea Embayment promotes ice-sheet stability, *Science*, 360, 1335–1339, 2018.
- 385 Cornford, S. L., Martin, D. F., Payne, A. J., Ng, E. G., Le Brocq, A. M., Gladstone, R. M., Edwards, T. L., Shannon, S. R., Agosta, C., Van Den Broeke, M. R., Hellmer, H. H., Krinner, G., Ligtenberg, S. R. M., Timmermann, R., and Vaughan, D. G.: Century-scale simulations of the response of the West Antarctic Ice Sheet to a warming climate, *The Cryosphere*, 9, 1579–1600, <http://www.the-cryosphere.net/9/1579/2015/tc-9-1579-2015-supplement.zip>, 2015.
- De Rydt, J., Gudmundsson, G., Rott, H., and Bamber, J.: Modeling the instantaneous response of glaciers after the collapse of the Larsen B
390 Ice Shelf, *Geophysical Research Letters*, 42, 5355–5363, 2015.
- Fretwell, P., Pritchard, H. D., Vaughan, D. G., Bamber, J., Barrand, N., Bell, R., Bianchi, C., Bingham, R., Blankenship, D., Casassa, G., et al.: Bedmap2: improved ice bed, surface and thickness datasets for Antarctica, *The Cryosphere*, 7, 375–393, <https://doi.org/10.5194/tc-7-375-2013>, 2013.
- Fürst, J. J., Durand, G., Gillet-Chaulet, F., Tavard, L., Rankl, M., Braun, M., and Gagliardini, O.: The safety band of Antarctic ice shelves,
395 *Nature Climate Change*, 6, 479, 2016.
- Gagliardini, O., Durand, G., Zwinger, T., Hindmarsh, R., and Le Meur, E.: Coupling of ice-shelf melting and buttressing is a key process in ice-sheets dynamics, *Geophysical Research Letters*, 37, 2010.
- Goldberg, D. N., Gourmelen, N., Kimura, S., Millan, R., and Snow, K.: How Accurately Should We Model Ice Shelf Melt Rates?, *Geophysical Research Letters*, 46, 189–199, <https://doi.org/10.1029/2018GL080383>, 2019.
- 400 Gudmundsson, G.: Ice-shelf buttressing and the stability of marine ice sheets, *The Cryosphere*, 7, 647–655, 2013.
- Gudmundsson, G. H.: Transmission of basal variability to a glacier surface, *Journal of Geophysical Research: Solid Earth*, 108, 2003.
- Gudmundsson, H., Krug, J., Durand, G., Favier, L., and Gagliardini, O.: The stability of grounding lines on retrograde slopes, *The Cryosphere*, 6, 1497–1505, 2012.
- Hoffman, M. J., Perego, M., Price, S. F., Lipscomb, W. H., Zhang, T., Jacobsen, D., Tezaur, I., Salinger, A. G., Tuminaro, R., and Bertagna,
405 L.: MPAS-Albany Land Ice (MALI): a variable-resolution ice sheet model for Earth system modeling using Voronoi grids, *Geoscientific Model Development*, 11, 3747–3780, <https://doi.org/10.5194/gmd-11-3747-2018>, <https://www.geosci-model-dev.net/11/3747/2018/>, 2018.
- Hutter, K.: Theoretical glaciology, Reidel Publ., Dordrecht, Netherlands, <https://doi.org/10.1007/978-94-015-1167-4>, 1983.
- Jenkins, A., Dutrieux, P., Jacobs, S., Steig, E., Gudmundsson, H., Smith, J., and Heywood, K.: Decadal Ocean Forcing and Antarctic
410 Ice Sheet Response: Lessons from the Amundsen Sea, *Oceanography*, 29, 106–117, <https://doi.org/10.5670/oceanog.2016.103>, <http://gateway.webofknowledge.com/gateway/Gateway.cgi?GWVersion=2&SrcAuth=mekentosj&SrcApp=Papers&DestLinkType=FullRecord&DestApp=WOS&KeyUT=000390560400013>, 2016.
- Joughin, I., Smith, B. E., and Medley, B.: Marine ice sheet collapse potentially under way for the Thwaites Glacier Basin, West Antarctica,
415 Science, 344, 735–738, 2014.

- 415 Lick, W.: The propagation of disturbances on glaciers, *Journal of Geophysical Research*, 75, 2189–2197, 1970.
- Liefferinge, B. V. and Pattyn, F.: Using ice-flow models to evaluate potential sites of million year-old ice in Antarctica, *Climate of the Past*, 9, 2335–2345, 2013.
- Mercer, J. H.: West Antarctic ice sheet and CO₂ greenhouse effect: a threat of disaster, *Nature*, 271, 321, 1978.
- Morland, L.: Unconfined ice-shelf flow, in: *Dynamics of the West Antarctic Ice Sheet*, pp. 99–116, Springer, 1987.
- 420 Pegler, S. S. and Worster, M. G.: Dynamics of a viscous layer flowing radially over an inviscid ocean, *Journal of Fluid Mechanics*, 696, 152–174, 2012.
- Perego, M., Gunzburger, M., and Burkardt, J.: Parallel finite-element implementation for higher-order ice-sheet models, *Journal of Glaciology*, 58, 76–88, <https://doi.org/10.3189/2012JoG11J063>, 2012.
- Perego, M., Price, S., and Stadler, G.: Optimal initial conditions for coupling ice sheet models to Earth system models, *Journal of Geophysical Research: Earth Surface*, 119, 1894–1917, 2014.
- 425 Reese, R., Gudmundsson, G. H., Levermann, A., and Winkelmann, R.: The far reach of ice-shelf thinning in Antarctica, *Nature Climate Change*, 8, 53, 2018.
- Rignot, E., Mouginot, J., Morlighem, M., Seroussi, H., and Scheuchl, B.: Widespread, rapid grounding line retreat of Pine Island, Thwaites, Smith, and Kohler glaciers, West Antarctica, from 1992 to 2011, *Geophysical Research Letters*, 41, 3502–3509, 2014.
- 430 Royston, S. and Gudmundsson, G. H.: Changes in ice-shelf buttressing following the collapse of Larsen A Ice Shelf, Antarctica, and the resulting impact on tributaries, *Journal of Glaciology*, 62, 905–911, 2016.
- Schoof, C.: Ice sheet grounding line dynamics: Steady states, stability, and hysteresis, *Journal of Geophysical Research: Earth Surface*, 112, 2007.
- Schoof, C.: Marine ice sheet stability, *Journal of Fluid Mechanics*, 698, 62–72, 2012.
- 435 Schoof, C. and Hewitt, I.: Ice-sheet dynamics, *Annual Review of Fluid Mechanics*, 45, 217–239, 2013.
- Seroussi, H., Morlighem, M., Larour, E., Rignot, E., and Khazendar, A.: Hydrostatic grounding line parameterization in ice sheet models, *The Cryosphere*, 8, 2075–2087, 2014.
- Tezaur, I. K., Perego, M., Salinger, A. G., Tuminaro, R. S., and Price, S.: Albany/FELIX: a parallel, scalable and robust, finite element, first-order Stokes approximation ice sheet solver built for advanced analysis, *Geoscientific Model Development*, 8, 1–24, <https://doi.org/10.5194/gmd-8-1-2015>, 2015a.
- 440 Tezaur, I. K., Tuminaro, R. S., Perego, M., Salinger, A. G., and Price, S. F.: On the Scalability of the Albany/FELIX first-order Stokes Approximation ice Sheet Solver for Large-Scale Simulations of the Greenland and Antarctic ice Sheets, *Procedia Computer Science*, 51, 2026–2035, <https://doi.org/10.1016/j.procs.2015.05.467>, 2015b.
- Wearing, M.: The Flow Dynamics and Buttressing of Ice Shelves, Ph.D. thesis, University of Cambridge, 2016.

445 **Appendix A: Appendix materials**

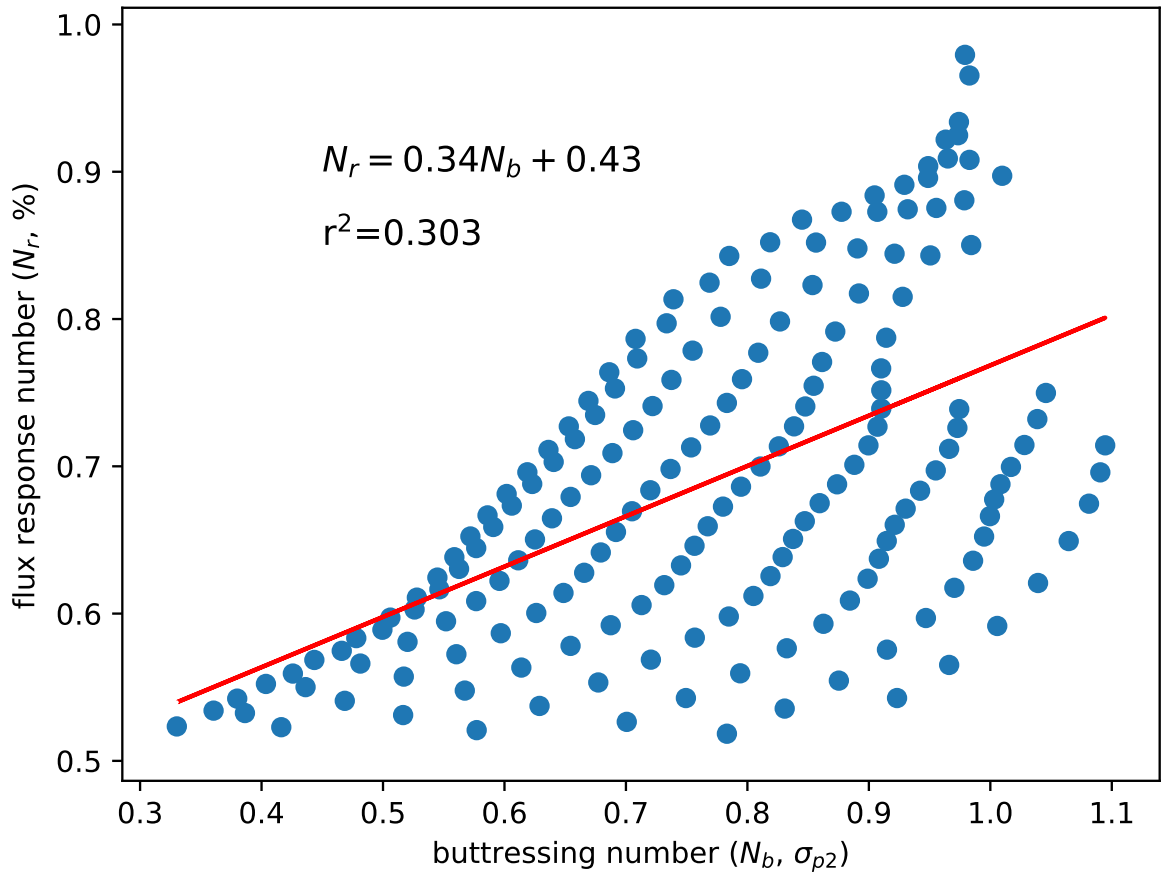


Figure A1. $N_b:N_r$ correlation for perturbation points within the confined region of the shelf and with a thickness gradient magnitude $|\nabla H| < 7 \times 10^{-3}$. N_b is calculated from the second principal stress σ_{p2} .

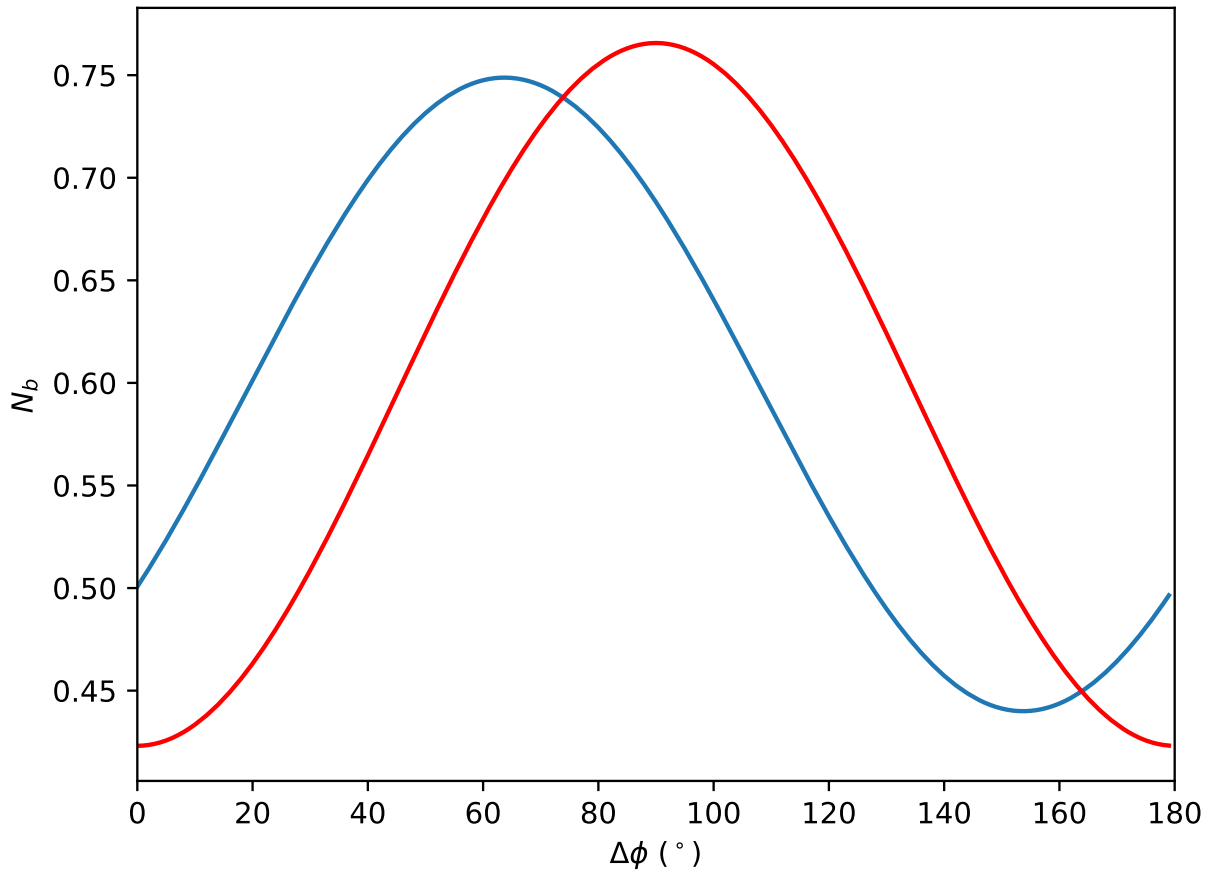


Figure A2. N_b values rotated counterclockwise by $\Delta\phi$ degrees relative to the σ_{p1} direction (red) and the ice flow direction (blue). It's a twin plot for Fig. 2a. Both curves show the buttressing number is largest along the σ_{p2} direction.

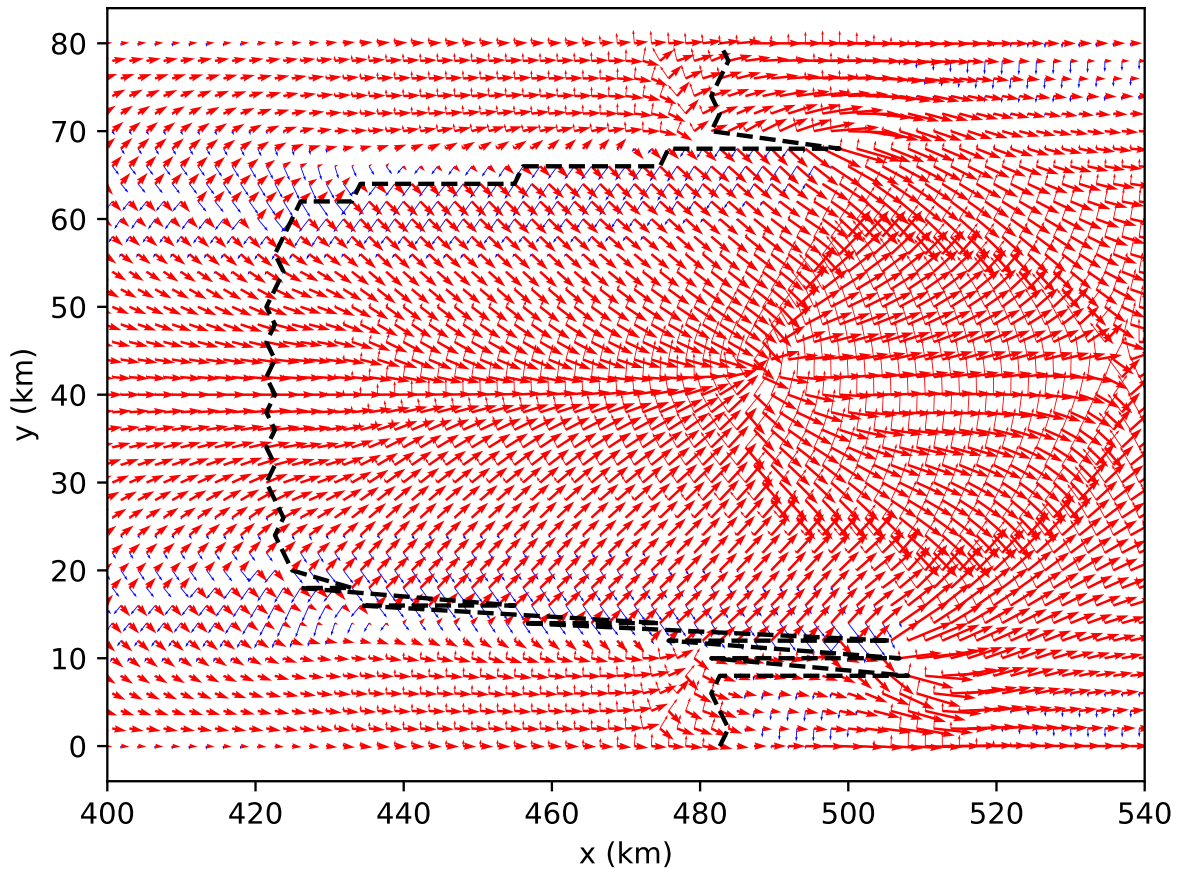


Figure A3. The quiver plot of σ_{p1} (thick arrows) and σ_{p2} (thin arrows) field. The red and blue colors means tensile and compressive stress, respectively. The thick dashed black line represents the grounding line.

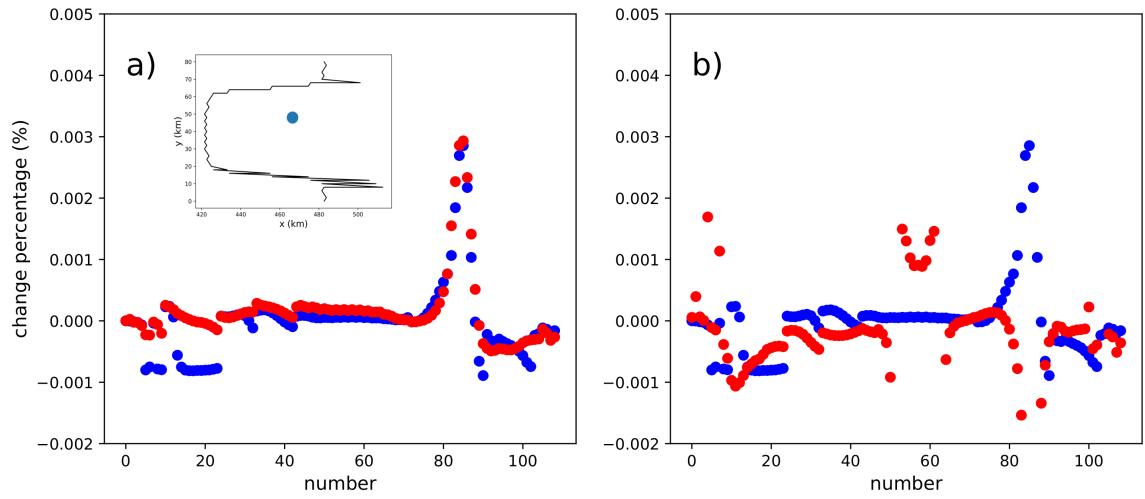


Figure A4. Relationship between changes in velocity (blue) and changes in the stress (red) along the GL for the MISMIP+ test case, due to a perturbation at a specific location on the ice shelf (blue dot in inset map). In a), changes in GL velocities are plotted against changes in σ_{p1} . In b), changes in GL velocity are plotted against changes in σ_{p2} . The *x*-axis represents an index for the grid cell number along the GL.

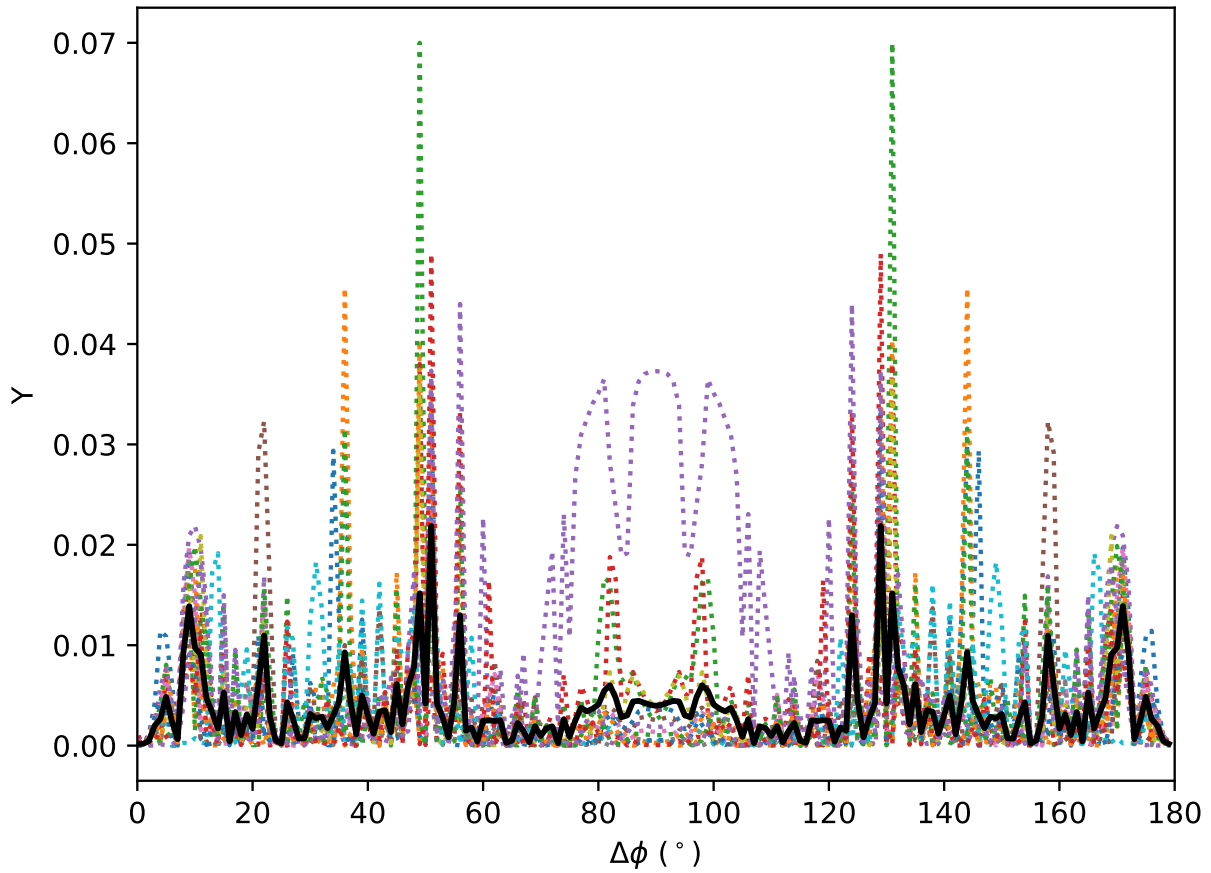


Figure A5. The correlation (Υ) between the changes of ice surface speed and the changes of normal stress along GL for the Larsen C experiments. The direction of normal stress is rotated counterclockwise from the direction of σ_{p1} . The colored dashed curve each represents a perturbation experiment, and the thick back curve is their mean value.

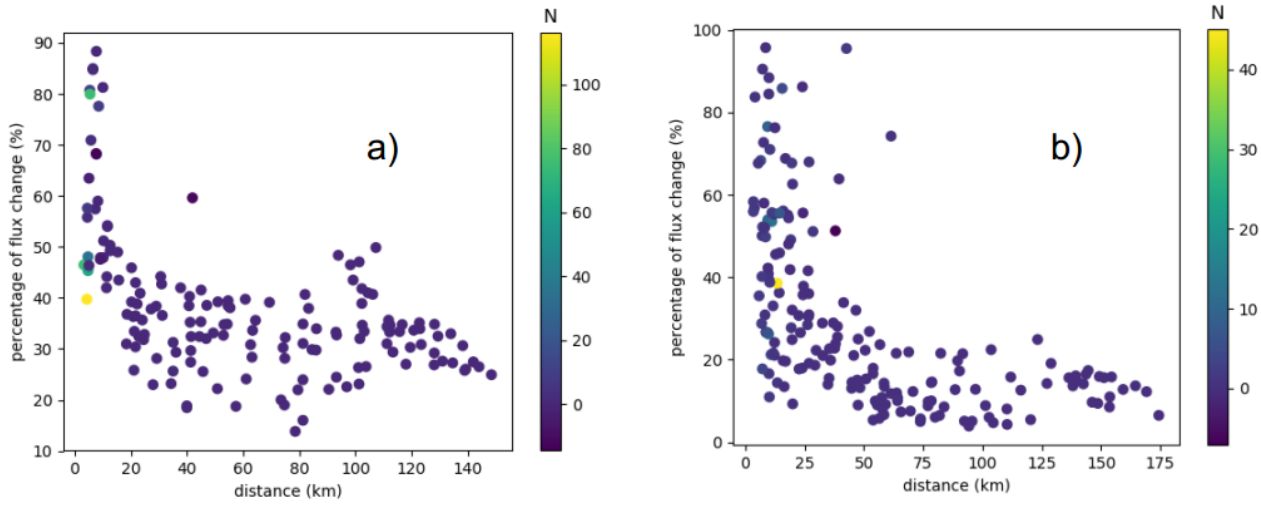


Figure A6. At each perturbation point, we locate the 5 closest GL cells and calculate the percentage (*y*-axis) of the total GL flux due to those 5 cells for a) MISMIP+ and b) Larsen C. The *x*-axis is the distance between the perturbation point and those 5 cells. The percentage is largest when the distance between the GL and the perturbation is small, supporting the concept that perturbations near the GL, in general, have a larger impact on the nearby flux across the GL. The colorbar shows the buttressing number.

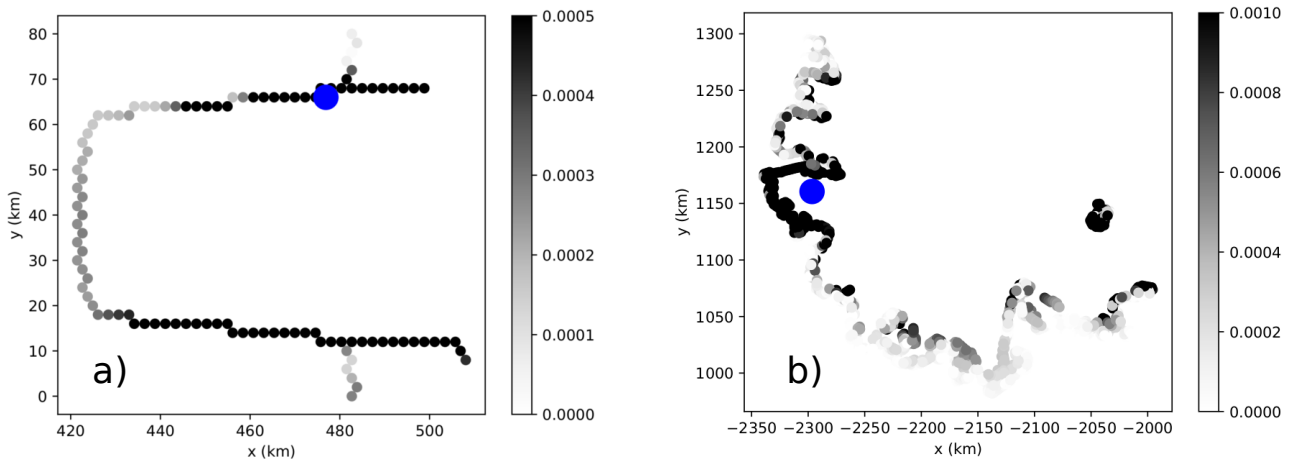


Figure A7. The ice surface speed change (%) along grounding line under certain specified perturbation locations for MISMIP+ (a) and Larsen C (b).

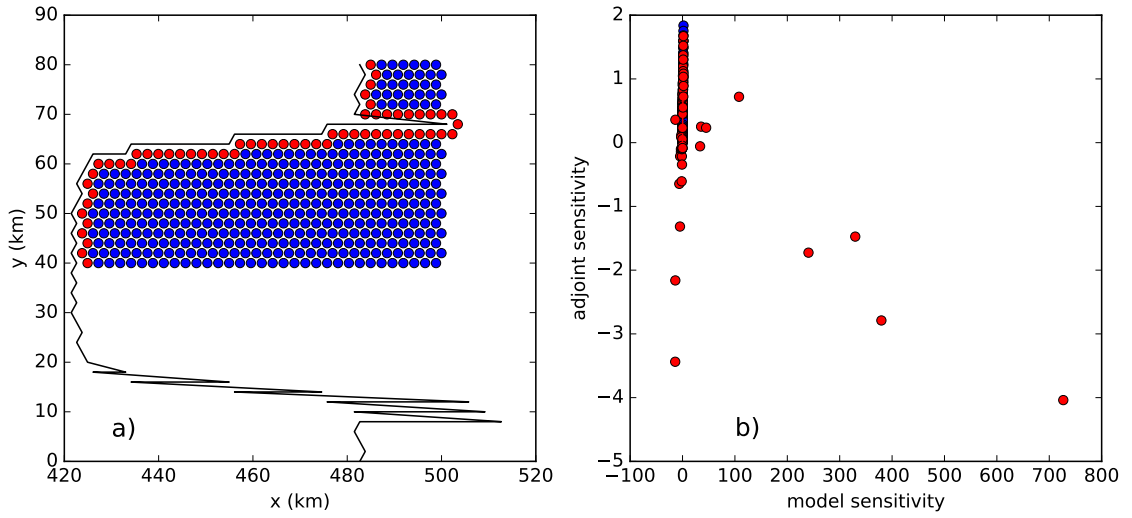


Figure A8. Grounding line flux sensitivity for the MISMIP+ domain calculated from individual perturbation experiments versus derived from a model adjoint (perturbation locations are shown by circles in a). Perturbation-experiment (x-axis) and adjoint-derived (y-axis) sensitivities (see text for definition) are plotted against one another in b). In a and b, the red circles indicate near-GL (<2 km) perturbation points, which are omitted in the comparison in Fig. 11. The GL in a) is shown by the black curve. In b), the red line is a linear regression between the perturbation-experiment and adjoint-derived sensitivities.